JACS
JOURNAL OF THE AMERICAN CHEMICAL SOCIETY
pubs.acs.org/JACS
Article

Dynamic Competition between Hubbard and Superexchange Interactions Selectively Localizes Electrons and Holes through Polarons

Jocelyn L. Mendes, Hyun Jun Shin, Jae Yeon Seo, Nara Lee, Young Jai Choi, Joel B. Varley, and Scott K. Cushing*

ABSTRACT: Controlling the effects of photoexcited polarons in transition metal oxides can enable the long time-scale charge separation necessary for renewable energy applications and controlling new quantum phases through dynamically tunable electron−phonon coupling. In previously studied transition metal oxides, polaron formation is facilitated by a photoexcited ligand-to-metal charge transfer (LMCT). When the polaron is formed, oxygen atoms move away from iron centers, which increases carrier localization at the metal center and decreases charge hopping. Studies of yttrium iron garnet and erbium iron oxide have suggested that strong electron and spin correlations can modulate photoexcited polaron formation. To understand the interplay between strong spin and electronic correlations in highly polar materials, we studied gadolinium iron oxide ($GdFeO_3$), which selectively forms photoexcited polarons through an Fe−O−Fe superexchange interaction. Excitation-wavelength-dependent transient extreme ultraviolet (XUV) spectroscopy selectively excites LMCT and metal-to-metal charge transfer (MMCT) transitions. The LMCT transition suppresses photoexcited polaron formation due to the balance between superexchange and Hubbard interactions, while MMCT transitions result in photoexcited polaron formation within 250 ± 40 fs. Ab initio theory demonstrates that electron and hole polarons localize on iron centers following MMCT. In addition to understanding how strong electronic and spin correlations can control strong electron−phonon coupling, these experiments separately measure electron and hole polaron interactions on neighboring metal centers for the first time, providing insight into a large range of charge-transfer and Mott−Hubbard insulators.

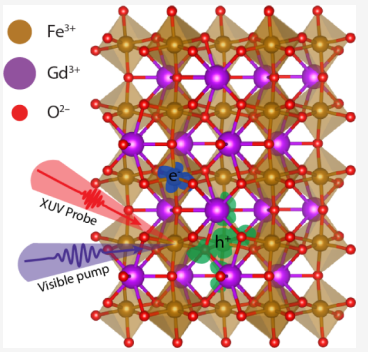

INTRODUCTION

Polaron formation in transition metal oxide materials has been widely explored for its effects on ground-state transport in correlated materials and solar energy processes like photocatalysis.[1−5] In highly polar materials, the coupling of photoexcited charge carriers to phonons in the lattice localizes carriers in the form of polarons.[6] Parameters to dynamically control laser-driven strong electron−phonon coupling is an ongoing search. Understanding and controlling the underlying physics that determines the formation of polarons in materials could provide meaningful improvements to a wide range of material classes, from organic electronics to solar energy systems and exotic quantum phases.[7,8]

Hematite (α-Fe_2O_3) and other iron oxides have been extensively explored for their photoexcited polaron formation dynamics.[9−12] Most of these materials are charge-transfer insulators, where the valence band maximum (VBM) is dominated by O 2p orbitals, and the conduction band minimum (CBM) is dominated by metal 3d orbitals. An above-band gap photoexcitation induces a ligand-to-metal charge transfer (LMCT) transition from oxygen to the metal center. The electronic structures of metal oxides also span intermediate and Mott−Hubbard insulators, where the VBM is dominated by either mixed oxygen/metal orbitals or entirely metal orbitals, respectively. These differing electronic structures pose a unique route for the modulation of carrier localization by polaron formation following photoexcitation.

Almost uniformly across iron oxides, photoexcited small polaron formation occurs within a few hundred femtoseconds of the charge transfer transition.[10,13,14] A subsequent expansion of Fe−O bond lengths and localization of electron density on polaronic iron sites has been measured using a variety of X-ray spectroscopies. Recent work exploring the tunability of polaronic properties has been demonstrated using structural distortions and strong electron and spin correlations. For example, rare-earth orthoferrite $ErFeO_3$ was found to have weaker polaronic binding energies because the polaron formation rate was slowed by strong electronic correlations.[12]

Received: November 26, 2024
Revised: April 21, 2025
Accepted: April 22, 2025

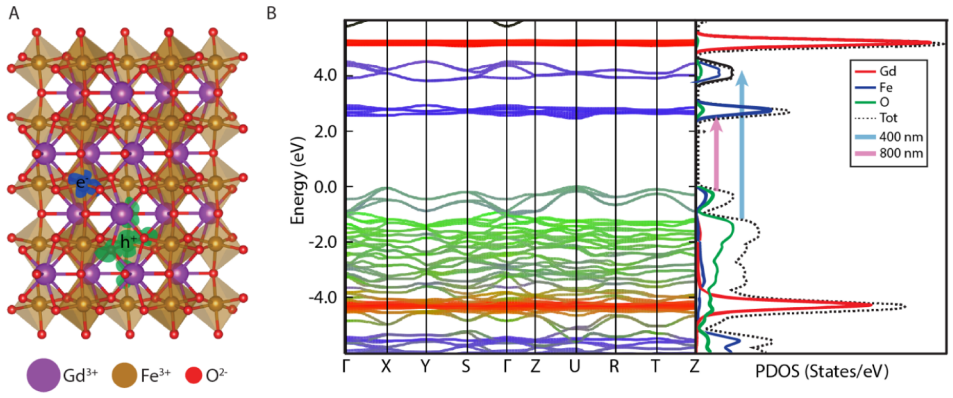

Figure 1. (A) $GdFeO_3$ crystal structure with electron (blue) and hole (green) polaron charge densities as calculated with exchange correlation functionals that correct for self-interaction errors, referred to as defect supercell calculations. The electron and hole polarons are both predicted to be centered on iron atoms. (B) Calculated electronic band structure and the projected density of states (PDOS) with the HSE06 hybrid functional with 15% exact exchange for the studied AFM ground state, including tentative assignments of band transitions associated with the 800 nm (pink arrow) and 400 nm (blue arrow) excitations that lead to the polaron formation. The bandgap is overestimated due to deficiencies associated with the DFT of transition metals, but the band structure and contributions of relative orbitals are preserved. The excitation arrows are adjusted accordingly to showcase the transition densities expected based upon the experimentally measured band gap.

Additional work comparing hematite and $Y_3Fe_5O_{12}$ (YIG) finds that strong spin-selective dynamics reduce polaron formation in YIG and increase its photocatalytic efficiency by an order of magnitude with respect to hematite.[15] Transient XUV and X-ray spectroscopies, however, have yet to be applied to the simultaneous measurement of electron and hole polarons in intermediate and Mott−Hubbard insulating iron oxides.

Here, we employ excitation-wavelength-dependent transient extreme ultraviolet (XUV) reflection spectroscopy to explore the relation between superexchange and Hubbard interactions in influencing strong carrier localization through polarons in single-crystal rare-earth orthoferrite $GdFeO_3$. This intermediate insulator (mixed O 2p/Fe 3d VBM) is a model material system for many perovskite Mott−Hubbard insulators due to its crystal structure.[16,17] $GdFeO_3$ and other rare-earth orthoferrites have been explored as candidates for photoelectrochemical oxygen reduction and evolution, as well as magneto-optical and spintronic applications due to their demonstrated multiferroicity.[18,19] Through transient XUV spectroscopy, we find that LMCT from O 2p to Fe 3d orbitals results in the suppression of photoexcited polaron formation, while a metal-to-metal charge transfer (MMCT) induces photoexcited polaron formation. The MMCT enables polarons by superexchange across an Fe−O−Fe bond, resulting in hole and electron polarons localized on neighboring iron centers, and a reduced radiative lifetime (<100 ps for MMCT versus 1.2 ± 0.4 ns for LMCT). Polaron formation is suppressed following a higher energy LMCT due to the balance of on-site Coulomb repulsion (U) from oxygen-dominated valence orbitals and superexchange in the final spin state. While thermalization of these carriers occurs in ∼350 fs, the final spin state from the LMCT prevents the polaron formation. Ab initio density functional theory (DFT) and the Bethe−Salpeter equation (BSE) simulate the photoexcited XUV dynamics. Polaron-induced lattice distortions and charge localization within a defect supercell approach were assessed with different levels of electronic structure theory, ranging from DFT incorporating on-site Hubbard U parameters with variational polaron self-interaction-corrected (pSIC) total-energy functional models to hybrid functionals with different fractions of exact exchange. The results provide new insight into tuning polaronic properties via strong electronic and spin correlations for transition metal oxide materials, particularly identifying superexchange interactions as a new dynamical carrier localization and polaron design parameter.

EXPERIMENTAL SECTION

Synthesis of Single-Crystalline $GdFeO_3$. Single crystals of $GdFeO_3$ were synthesized using the flux method, employing PbO, PbF_2, PbO_2, and B_2O_3 as fluxes in a high-temperature furnace. A stoichiometric mixture of Gd_2O_3 and Fe_2O_3 powders was thoroughly combined with the flux compounds and placed in a platinum crucible. The mixture was heated to 1250 °C for 16 h to ensure complete dissolution. Then, it was cooled slowly to 850 °C at a rate of 2 °C/h, and further cooled to room temperature at a rate of 100 °C/h. This process yielded large cuboid shaped $GdFeO_3$ crystals, with individual crystals obtaining lengths of up to 1 cm on a side. Characterization of the $GdFeO_3$ single crystals can be found in the Supporting Information.

Transient Extreme Ultraviolet (XUV) Spectroscopy. For both photoexcitation wavelengths, the pump pulses are ∼50 fs with a fluence of ∼11 mJ/cm^2 and are time-delayed with respect to the probe pulse. In the case of 800 nm photoexcitation, this results in a photoexcited carrier density of $\sim 7.3 \times 10^{20}$ cm^{-3}, and for 400 nm excitation a carrier density of $\sim 3.7 \times 10^{20}$ cm^{-3}, details of the carrier density calculation can be found in the Supporting Information. The DFT-calculated unit cell of $GdFeO_3$ has a volume of $\sim 2.4 \times 10^{-22}$ cm^3 and given that each unit cell contains 4 iron atoms, there are approximately $\sim 1.6 \times 10^{22}$ Fe atoms/cm^3. This would result in ∼4.5% and ∼2.3% of iron atoms excited following 800 and 400 nm photoexcitation, respectively. The XUV probe pulse is generated by high harmonic generation in Ar gas from a few-cycle white light pulse. The transient extreme ultraviolet reflection experiment employs a 10° grazing incidence geometry, which results in a ∼2 nm penetration depth.[20] The Fe $M_{2,3}$ edge at ∼54 eV corresponds to transitions from the $3p_{3/2,5/2}$ core levels into 3d core levels. The change in transient reflection following photoexcitation is defined by $\Delta OD = -\log_{10}(I_{pump\ on}/I_{pump\ off})$. Additional details about the transient extreme ultraviolet spectrometer can be found in the Supporting Information.

Ab Initio Polaron and Core-Level Spectra Modeling. The theoretical framework we employ to fully analyze the transient core-level spectra has been described in detail previously.[21] We compute both the ground-state X-ray absorption at the Fe $M_{2,3}$ edge in $GdFeO_3$ and differential effects to the core-level $GdFeO_3$ spectra following excitation-wavelength-dependent photoexcitation and polar-

on formation. These effects are calculated with an ab initio theoretical approach which employs density functional theory and the Bethe–Salpeter equation (DFT+BSE). The DFT+BSE approach employs DFT using the Quantum ESPRESSO package[22,23] and the existing OCEAN code[24−26] (Obtaining Core-level Excitations using Ab-initio calculations and the NIST BSE solver). We have modified the BSE to use excited state distributions to determine transient changes in the XUV spectra. We first calculate the band structure of $GdFeO_3$ using DFT. Then, the BSE is solved to obtain the core–valence exciton wave functions and transient XUV spectra can be plotted from the complex dielectric function calculated by OCEAN. A modification to the OCEAN code, discussed previously,[21,27] is employed to model the initial 800 nm MMCT and 400 nm LMCT states.

Polaronic distortions are modeled using a DFT+BSE approach where we apply a semiempirical distortion to an FeO_6 octahedra and calculate its resulting Fe $M_{2,3}$ edge spectra. Polaronic distortions calculated using this technique are termed DFT+BSE. The polaronic distortions are modeled independently of the different charge transfer transitions, but it is implied that only MMCT could induce hole polarons on iron centers. We further model polaronic lattice distortions using a defect supercell approach with hybrid and polaron self-interaction corrected exchange-correlation functionals (HSE06 and pSIC) as implemented in the VASP code.[28−32] These functionals either incorporate a fraction of Hartree–Fock (HF) exact exchange to improve self-interaction errors and a description of charge localization (e.g., hybrid functionals) that depends on an empirical parameter (α, the HF mixing parameter), or employ a variational approach from a closed-shell system for a parameter-free ab initio methodology for calculating polaron properties that removes the sensitivity to empirical parameters like α or Hubbard U parameters.[29] These methods were used to identify structural distortions and relative energetics associated with electron and hole polaron formation at different sites in $GdFeO_3$ and to assess their sensitivity to empirical parameters in the calculations. We generally refer to the polaron-containing structures and subsequent X-ray spectra obtained via these approaches (hybrid functionals and/or with the pSIC approach) as pSIC+DFT+BSE. Additional details about ab initio modeling of photoexcited XUV dynamics can be found in the Supporting Information section.

RESULTS AND DISCUSSION

Defect Supercell Calculations of Polarons. $GdFeO_3$ has an orthorhombic symmetry in the *Pbnm* space group, as shown in Figure 1A.[17] The FeO_6 octahedra are strained due to the large rare-earth atom in the crystal structure, resulting in a 154° Fe–O–Fe bond angle.[33] Strong electron correlations introduced by both the Fe d and Gd f orbitals enable a mixed Fe d/O p band at the VBM and a metal d band at the CBM, as shown in Figure 1B. This contrasts with previously measured iron oxides whose density of states follow a charge-transfer insulating structure where the VBM is dominated by O 2p orbitals.[10,21] DFT+U is used to accurately describe the extent of carrier localization and on-site repulsion in $GdFeO_3$.[17] Magnetization studies of $GdFeO_3$ have demonstrated that it is a canted, G-type antiferromagnet (AFM) below its Néel temperature (T_N) of ∼650 K, resulting in a weak ferromagnetism due to the Dzyaloshinskii–Moriya (DM) interaction.[34−36] The Fe^{3+} ions in the $GdFeO_3$ take a high-spin (HS) electronic configuration in their ground state, and the octahedral tilts of adjacent FeO_6 octahedra are measured to have strong antisymmetric exchange interactions (superexchange).[37,38]

Figure 1B shows the two photoexcitation pathways used in the excitation-wavelength-dependent XUV measurements. In the case of the 400 nm (3.1 eV) photoexcitation, carriers are excited from lower-lying valence bands that are dominated by O 2p orbitals into higher-energy Fe 3d and Gd 6f orbital-dominated conduction bands. Photoexcitation with 400 nm light follows a LMCT mechanism. The lower-energy 800 nm (1.55 eV) photoexcitation induces transitions from the VBM, which are mixed in O 2p and Fe 3d orbital character, into lower-energy conduction bands dominated by Fe 3d orbitals. The mixed nature of the VBM in $GdFeO_3$ poses an opportunity for both MMCT and LMCT to occur.[39] These excitation energies provide different possible pathways for polaron formation.

We employ a defect supercell approach with hybrid and polaron self-interaction corrected exchange-correlation functionals (HSE06 and pSIC) to calculate ab initio polaronic distortions in $GdFeO_3$. Further details of the calculations can be found in the Experimental section and the Supporting Information. These methods identify structural distortions and relative energetics associated with electron and hole polaron formation at different sites in $GdFeO_3$ and assess their sensitivity to empirical parameters in the calculations. The charge localization of both electron and hole polarons from defect supercell calculations (Figure 1A) predicts that the electron polaron localizes on one single iron site. The hole polaron is less localized than the electron polaron; however, its charge density is predicted to be centered over an iron site as well. A polaron formed following MMCT would induce both electron and hole polaron formation on iron centers. We hypothesize that the lack of an oxygen-centered polaron from the mixed orbital VB means that the LMCT may not lead to polaron formation.

Hubbard-Holstein Model of Polaron Formation. To understand the defect supercell-predicted localization of electron and hole polarons on iron centers in $GdFeO_3$, we must understand the conditions that make polaron formation favorable in a material system. The model Hamiltonian that follows the two-site Hubbard–Holstein model in eq 1 presents the relevant properties that dictate polaron formation:

$$H = -t_{ij}\sum_{\langle ij\rangle\sigma}(c_{i\sigma}^{\dagger}c_{j\sigma} + H.\,C.\,) + U\sum_{i} n_{i\uparrow}n_{i\downarrow} + J\sum_{ij}\vec{S_i}\cdot\vec{S_j} + \omega_0\sum_{i} b_i^{\dagger}b_i + g\sum_{i,\sigma} n_{i\sigma}(b_i + b_i^{\dagger}) \quad (1)$$

where t_{ij} is the hopping integral, $c_{i\sigma}^{\dagger}$and $c_{j\sigma}$ are the creation and annihilation operators, respectively, with spin, σ, for an electron at site i and j.[40−45] U is the on-site Coulombic repulsion, n_i is the number operator, g corresponds to the electron–phonon coupling strength, and ω_0 refers to the phonon frequency. $b_i^{\dagger}$ and b_i are the creation and annihilation operators, respectively, for phonons at site i. J denotes the superexchange interaction between neighboring metal sites.[46] The Hubbard–Holstein Hamiltonian is commonly down-folded to a t–J model.[47,48] Here we consider the Hubbard–Holstein model for simplicity, but a t-J Hamiltonian could be applied under certain coupling regimes.

Polarons exist in a strongly electron–phonon coupled regime, as carriers are localized by strong interactions with the lattice. Alternatively, when electron–phonon coupling is sufficiently weak, carriers may conduct freely in materials and polaron formation is suppressed. This indicates that for polaron formation to be favorable $t \ll g$, while polaron formation would be weak or suppressed when $t \gg g$. In a $U \gg t$ regime at half-filling, $J \approx 4t^2/U$, and for an antiferromagnet $t_{eff} \propto J$ and $t_{eff} \propto 1/U$.[46,49,50] We note that this is an

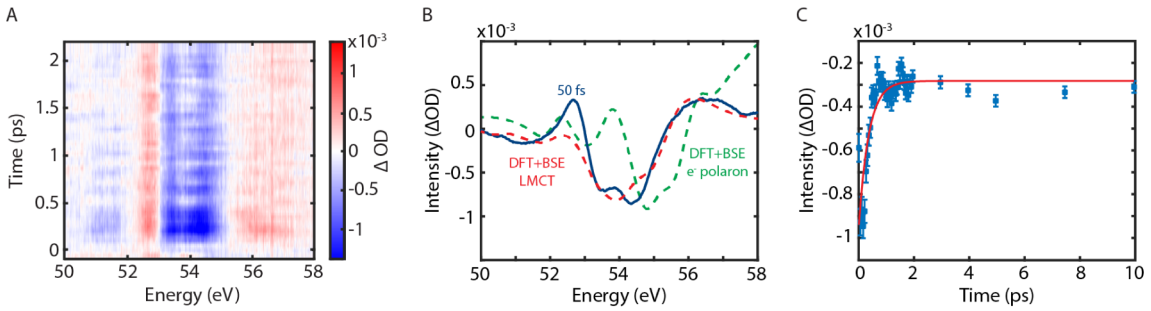

Figure 2. (A) Transient XUV spectra following 400 nm photoexcitation. (B) Experimental lineout from 50 fs after 400 nm photoexcitation (blue) compared to DFT+BSE theory lineouts that model the 400 nm LMCT state (red) and an electron polaron state on an iron atom (green) show agreement with a LMCT state following 400 nm photoexcitation. (C) Fitting of the thermalization at the Fe $M_{2,3}$ edge following 400 nm photoexcitation, averaged over the Fe $M_{2,3}$ edge feature.

oversimplification, as U and J are changing many body wave functions. DMFT work to study the interplay of electron−phonon coupling and the superexchange interaction find that as g increases, J decreases, meaning that superexchange is suppressed in a strongly electron−phonon coupled regime.[41] On-site Coulombic repulsions are inversely related to J, and thus, J is also expected to be suppressed in a regime where U is sufficiently large.[46]

The defect supercell calculations of $GdFeO_3$ predict that both electron and hole polarons will form on metal sites (Figure 1A). This contradicts previous measurements of polaron formation, in which the hole polaron would be localized on a ligand site and the electron polaron would be localized on a metal site. We hypothesize that this is primarily due to the different accessible excitation manifolds within this intermediate insulator. $GdFeO_3$ is expected to have strong J in its ground state due to the AFM configuration of adjacent Fe sites and the tilted FeO_6 octahedra.[38] However, the strong U associated with an MMCT will decrease charge hopping and increase the likelihood of polaron formation. On the other hand, LMCT would originate from a ligand with weak U, which would be associated with weakened electron−phonon coupling. In this case, charge hopping would be expected to be strong, and polaron formation will be suppressed.

Suppressed Polaron Formation Following LMCT. XUV spectroscopy has been employed extensively for the measurement of photoexcited polaron formation dynamics because it can evaluate ultrafast, element-specific electronic-structural dynamics.[9,10,14] Spectrally, polaron formation in iron oxide materials has been characterized in the XUV as a shift to higher energies at the Fe $M_{2,3}$ edge. As carriers localize on the iron center, more energy is required to induce the core-to-valence 3p to 3d transition at the iron site. This has held for charge-transfer polarons across Fe−O materials with dynamics that agree well with transient X-ray diffraction and ultrafast optical techniques.[51,52]

Transient XUV reflectivity at the Fe $M_{2,3}$ edge of $GdFeO_3$ pumped with 400 nm (3.1 eV) light is shown in Figure 2A. The Fe $M_{2,3}$ edge is characterized immediately after photoexcitation by a negative absorption feature (blue) centered around 54 eV. This spectral feature can be described by a reduction in the population of the Fe^{3+} ground state (Figure S4) as electrons are excited into Fe d orbitals in the $GdFeO_3$ conduction bands.[10] Transient increases in absorption are present in the 400 nm pumped spectra (Figure 2A) from ∼52.6−52.9 and ∼55.6−58.0 eV. Despite no spectral shift to higher energies being observed at the Fe $M_{2,3}$ edge following 400 nm photoexcitation, there is a decrease in intensity over time (Figure 2A). Figure 2C provides an exponential fit of this decrease in intensity, resulting in a rate constant of $\tau_{400\text{ nm hot carriers}} = 360 \pm 70$ fs, which we attribute to the cooling rate of the hot carriers, in line with XUV studies of photoexcited carrier cooling.[20,53−55]

Due to the strong contribution of angular momentum to the core-level transition Hamiltonian at the Fe $M_{2,3}$ edge, increases (red) and decreases (blue) in absorption in the XUV spectrum do not directly relate to electron and hole energies following photoexcitation, but instead relate to changes in oxidation state, phonon modes, and other structural distortions such as small polarons.[10,12] To understand the origin of the spectral features at the Fe $M_{2,3}$ edge of $GdFeO_3$, we use a density functional theory and Bethe−Salpeter equation (DFT+BSE) approach to model the excited state X-ray edge dynamics. The method uses the Quantum ESPRESSO[22,23] and the OCEAN[24−26] (Obtaining Core Excitations from the Ab initio electronic structure and the NIST BSE solver) codes. Our defect supercell approach with hybrid and polaron self-interaction corrected exchange-correlation functionals (HSE06 and pSIC) calculates ab initio polaronic distortions in $GdFeO_3$ which are applied to our DFT+BSE framework (pSIC+DFT+BSE). We also model charge transfer and semiempirical polaronic states using this DFT+BSE approach. The theoretical methods applied here are discussed in more detail in the Experimental section and Supporting Information.

Figure 2B compares an experimental lineout following 400 nm photoexcitation with DFT+BSE theory modeled 400 nm LMCT and electron polaron states. There is good agreement between experimental lineouts at varying time delays following the 400 nm pump and the modeled 400 nm LMCT state. There is poor agreement between the 400 nm experimental lineouts and the DFT+BSE-modeled polaron state that shifts to higher energy. Furthermore, the increases in absorption following 400 nm photoexcitation (Figure 2A) from ∼52.6−52.9 and ∼55.6−58.0 eV are described by high-spin Fe^{2+} states forming as LMCT from the oxygen to iron atoms occurs (Figure 3A) using ligand-field multiplet theory.[56] A low-spin (LS) Fe^{2+} state does not agree with the experimentally measured spectrum (Figure 3A).

The photoexcited LMCT state occurs on the same time scale as the pulse width and is present up to our temporal detection limit of 1 ns (Figure S5B). The nonradiative recombination is, therefore, longer than our instrument's 1 ns temporal limit. An exponential fit of the radiative lifetime of $GdFeO_3$ gives a time constant of $\tau_{400\text{ nm radiative}} = 1.2 \pm 0.4$ ns

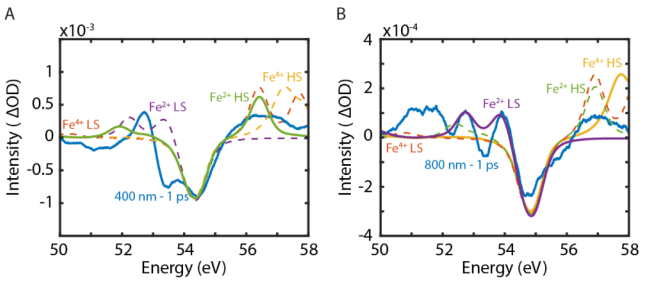

Figure 3. Experimental (blue) 400 nm LMCT state (A) and 800 nm polaron and trapped Fe^{2+} low-spin state (B). CTM4XAS calculated Fe^{4+} high-spin state (yellow), Fe^{4+} low-spin state (red), Fe^{2+} high-spin state (green), and Fe^{2+} low-spin state (purple). Each oxidation and spin state are plotted for comparison, but the solid lines refer to the assigned CTM4XAS calculated spin states for both experimental spectra.

(Figure S3), but we cannot confirm if the radiative lifetime is from defects or polarons based on our measurement limits. Further details of fluorescence lifetime measurements can be found in the Supporting Information.

If we consider the hot carrier thermalization from Figure 2C, with a time constant of $\tau_{400\text{ nm hot carriers}}$ = 360 ± 70 fs and compare it to the DFT-calculated phonon band dispersion for $GdFeO_3$, we can approximate the energetic extent of carrier cooling to the CBM. $GdFeO_3$ has its highest frequency phonon mode occurring around ∼17 THz, which corresponds to ∼70.3 meV.[57] At a first-order approximation, we can apply eq 2 to calculate the amount of energy the hot carriers cool by

$$\Delta E_{\text{hot carriers}} = \frac{\tau_{400\text{ nm hot carriers}}}{\tau_{e-ph}/2} \times E_{ph} \quad (2)$$

where E_{ph} is the highest frequency phonon mode and $\tau_{e\text{-}ph}$ is the electron−phonon scattering rate, which can also be approximated by the highest frequency phonon mode in the phonon band dispersion. The factor of 2 corresponds to the half phonon period frequency on which electron−phonon scattering occurs, a common approximation in literature.[58,59] This results in ∼750 meV of thermalization. The experimentally measured direct band gap of single crystal $GdFeO_3$ is ∼1.4 eV (Figure S1), so electrons excited by the 400 nm pump would be ∼2.2 eV above the VBM. This would indicate that excitations occur from ∼1 eV below the VBM and the PDOS demonstrates that oxygen orbitals dominate those valence bands (Figure 1B), which supports that a LMCT occurs following 400 nm photoexcitation.

Our DFT+BSE, ligand-field multiplet theory, and fluorescence lifetime measurements, therefore, support that LMCT following 400 nm photoexcitation forms a high-spin Fe^{2+} excited state, but strong coupling to phonons that would induce a polaronic lattice distortion is not present. The lack of a spectral shift to higher energies following 400 nm photoexcitation suggests that polaron formation is suppressed or so weak that it does not influence the transient spectra, and does not compete with the free carriers and their thermalization during the LMCT step (Figure 2B).[10,12]

Polaron Formation Following MMCT. Transient XUV reflectivity at the Fe $M_{2,3}$ edge of $GdFeO_3$ following 800 nm (1.55 eV) photoexcitation is shown in Figure 4. Like 400 nm pumped transient XUV reflectivity spectra, the Fe $M_{2,3}$ edge following an 800 nm pump is characterized immediately after photoexcitation by a negative absorption feature (blue)

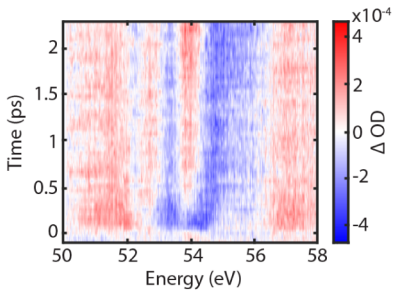

Figure 4. Transient XUV reflection−absorption spectrum following 800 nm photoexcitation.

centered around 54 eV. Unlike in the 400 nm spectra, the negative absorption feature pumped with 800 nm excitation has a spectral blueshift at the Fe $M_{2,3}$ edge from ∼52.8−55.8 eV (blue) that begins shortly after photoexcitation. This spectral shift is most prominent from ∼54.4−56.0 eV and has a time constant of 250 ± 40 fs (Figure S6) with an energy shift of 420 ± 150 meV. Following this spectral shift, a peak splitting results in a positive absorption feature (red, ∼53.5−54.3 eV) within the Fe $M_{2,3}$ edge in the 800 nm pumped spectra. Additionally, following 800 nm photoexcitation, an increase in absorption (Figure 4) that appears from ∼50.0−52.8 eV and ∼56.3−58.0 eV is measured.

The spectral lineout 50 fs after 800 nm photoexcitation in Figure 5A (blue) agrees well with DFT+BSE theory (red) for a

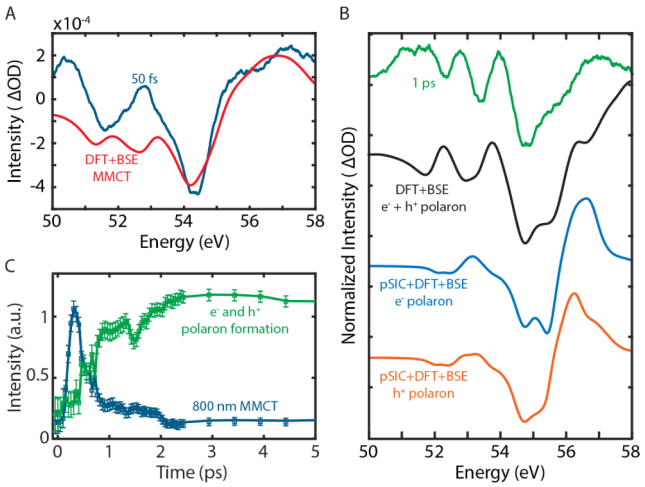

Figure 5. (A) Experimental lineout (blue) 50 fs after 800 nm photoexcitation and DFT+BSE theory calculated 800 nm MMCT state (red). (B) The polaron state that forms within a few hundred femtoseconds of 800 nm photoexcitation is modeled using DFT+BSE theory (black) for an electron and hole polaron and using the defect supercell pSIC+DFT+BSE theory for electron (blue) and hole (orange) polarons and is shown experimentally (green, 1 ps after 800 nm photoexcitation). Singular value decomposition (C) of the experimental 800 nm pumped transient spectra reveals the kinetics of photoexcited electron and hole polaron formation in $GdFeO_3$.

modeled 800 nm MMCT state. The DFT-calculated PDOS (Figure 1B) demonstrates that this excitation originates from mixed O 2p/Fe 3d valence bands and, therefore, could be either LMCT or MMCT in character. We find that the positive absorption features (Figure 4) at lower energies (∼50.0−52.8 eV) and higher energies (∼56.3−58.0 eV) in the 800 nm pumped spectra are associated with the creation of low-spin

Fe^{2+} and high-spin Fe^{4+} states, respectively (Figure 3B). The formation of high-spin Fe^{4+} states and low-spin Fe^{2+} states suggests that MMCT transitions are occurring between iron atoms following photoexcitation.[39] Section S5, in the Supporting Information, further discusses ligand-field multiplet theory to model these spin states.

Figure 5B shows agreement between the experiment after the blueshift (green), DFT+BSE theory for a convolved electron and hole polaron (black), and pSIC+DFT+BSE theory for both electron (blue) and hole (orange) polarons at neighboring iron sites. The pSIC+DFT+BSE-calculated electron and hole polarons occur at similar energies, suggesting that the electron and hole polarons are convolved spectrally. This confirms agreement between semiempirical DFT+BSE and ab initio pSIC+DFT+BSE theory, suggesting that different levels of theory can similarly describe the spectral shifts and features associated with convolved electron and hole polaron formation at the Fe $M_{2,3}$ edge. Singular value decomposition (SVD) in Figure 5C illustrates the transition of the MMCT state to the convolved electron and hole polaron state in the spectra. Figure S7 provides further details of the SVD analysis. The SVD plot demonstrates that the MMCT state transitions to the convolved electron and hole polaron state within the first picosecond following 800 nm photoexcitation. Long time-scale 800 nm XUV spectra (Figure S5A) reveal that the spectral shift lasts out to our instrument's temporal detection limit, and a fit of the exponential non-radiative decay reveals a time constant of 150 ± 30 ps.

Polaron Formation and Fe−O−Fe Superexchange. In addition to forming photoexcited electron and hole polarons on iron centers following 800 nm photoexcitation, a strong spectral splitting of the Fe $M_{2,3}$ edge feature occurs following polaron formation. The spectral splitting in the 800 nm spectra (Figure 4) results in an increase in absorption at ∼53.5−54.3 eV that arises 330 ± 50 fs following photoexcitation. In the transient XUV spectra following 400 nm photoexcitation (Figure 2A), there is spectral splitting that occurs at the Fe $M_{2,3}$ edge (53.8 eV), but it is weaker in intensity than the 800 nm photoexcitation, does not result in a positive signal, and does not change in intensity over time.

The spectral splitting can be attributed to t_{2g} and e_g crystal field splitting expected from the $GdFeO_3$ Fe^{3+} high-spin ground state (Figure S4).[37,60] This high-spin electronic configuration is preserved following 400 nm LMCT (Figure 3A), as demonstrated by the lack of change in spectral splitting between the ground state spectra and excited state 400 nm pumped spectra (Figures 2A and S4). Additionally, the increases in absorption following 400 nm photoexcitation (Figure 2A) result in the formation of an Fe^{2+} high-spin state, that appears as increases in absorption at ∼52.6−52.9 and ∼55.6−58 eV (Figure 3A). This indicates that the suppression of polaron formation following 400 nm photoexcitation is related to the preservation of the spin state of the iron atoms following LMCT. Furthermore, the LMCT state does not induce polaron formation because the electron density added to the iron atom originates from an oxygen atom. The ground state DFT predicted bond angle between Fe−O−Fe octahedra (∼147.1°) is highly conducive to superexchange. The Hubbard interaction is also weak on the oxygen atom. In this regime, the effective charge hopping integral, t_{eff}, remains large, suppressing polaron formation in the final, thermalized high spin state.

In the case of 800 nm photoexcitation, the strong electron−phonon coupling induced by photoexcited electron and hole polarons influences the dynamics of spectral splitting at the Fe $M_{2,3}$ edge. This is evidenced by the t_{2g} and e_g crystal field splitting in the 800 nm pumped spectra (Figure 4) experiencing a transient increase in absorption at ∼53.5−54.3 eV.[61] As demonstrated in the DFT+BSE and pSIC+DFT+BSE modeled spectra (Figure 5B), the Fe^{2+} and Fe^{4+} centers created following MMCT begin forming electron and hole polarons, respectively. The hole polaron charge density is distributed across the oxygen and Fe^{4+} iron atom, while the electron polaron charge density is localized on the Fe^{2+} site (Figure 1A). This is supported by ligand-field multiplet theory modeling of both high-spin and low-spin configurations of Fe^{2+} and Fe^{4+} (Figure 3B), that agrees well with a low-spin Fe^{2+} configuration following photoexcitation. The Fe^{4+} feature at higher energies does not experience this spectral splitting, which suggests that the iron that forms the hole polaron does not experience this spin crossover and remains in a high-spin configuration. This agrees with reports of delocalization, or "sharing", of holes across a metal and ligand participating in superexchange.[62,63]

The distortion induced by the polarons is anisotropic (Figure S10) and results in a Jahn−Teller distortion of the axial Fe−O ligands between the Fe−O−Fe bond length that is participating in polaron formation (Figure 6A). The Jahn−Teller effect has been demonstrated to induce changes to Fe−O−Fe bond angles that affect the superexchange interaction.[64−67] This oxygen-ligand-mediated superexchange enables spins that would have otherwise been misaligned in a high-spin state on the neighboring iron atoms to be transferred to a low-spin Fe^{2+} orbital configuration.[68] However, the bond angle is

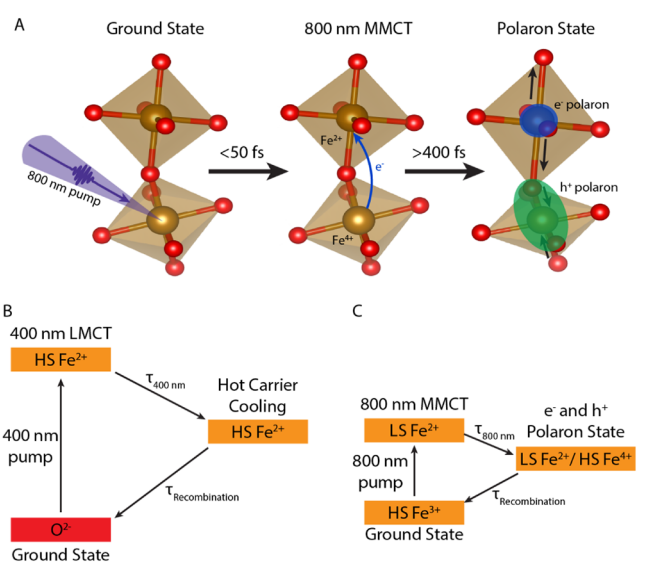

Figure 6. (A) Schematic of superexchange across the Fe−O−Fe bond that gives rise to spin crossover on Fe^{2+} centers during photoexcited electron and hole polaron formation. Within the first 50 fs, the 800 nm MMCT state results in a charge transfer from one iron center to another. After >400 fs, electron and hole polaron formation results in an expansion and contraction along the Fe−O−Fe bond length, which modulates its bond angle, inducing Jahn−Teller distortions and trapping the high-spin Fe^{2+} state. Diagram of the excitation pathways and spin manifolds present following both 400 nm (B) and 800 nm excitation (C). The fitting for the time constants for both hot carrier cooling following 400 nm LMCT ($\tau_{400\ nm}$ = 360 ± 70 fs) and polaron formation and superexchange following 800 nm MMCT ($\tau_{800\ nm}$ = 250 ± 40 fs) are discussed further in the Supporting Information.

reduced by ∼1.2° according to the DFT calculations, decreasing the superexchange and the effective charge hopping integral.[69−71] The Hubbard interaction is large for the MMCT between Fe centers and electron−phonon coupling can therefore dominate, resulting in polaron formation.

Iron oxides specifically have been reported to experience optical modification of the exchange interaction on sub-picosecond time scales, supporting this conclusion.[68] Particularly in the case of Mott insulators, whose VBM and CBM are dominated by metal orbitals, exchange interactions are calculated to be reversibly modulated by electric fields on ultrafast time scales.[42] The octahedral site distortion in rare-earth orthoferrites is responsible for orbital and spin ordering, the modulation of that distortion through polaron formation enables the trapping of a low-spin Fe^{2+} state induced by Fe−O−Fe superexchange following 800 nm MMCT.[71−73]

CONCLUSION

Excitation-wavelength-dependent small polaron formation is measured in the intermediate insulator $GdFeO_3$ using transient XUV reflection spectroscopy. Photoexcitation with an 800 nm pump results in both electron and hole polaron formation at neighboring iron sites and strong spectral splitting at the Fe $M_{2,3}$ edge, a spin crossover occurring on the iron atoms. A higher-energy 400 nm pump results in the suppression of polarons. This suggests a metal-metal polaron formation mechanism in which nearest-neighbor iron sites form a hole and electron polaron. The ability to modulate polaron formation by varying excitation wavelength has been studied previously in hematite.[10] However, this mostly results in changes to the polaron's mobility, lifetime, and recombination properties as carriers populate different energy levels of the conduction bands. In the case of $GdFeO_3$, we have suppressed photoexcited polaron formation with weak on-site repulsions following a higher-energy 400 nm photoexcitation, while inducing polaron formation when electron−phonon coupling is dominated by MMCT following 800 nm photoexcitation. The excitation-wavelength-dependent modulation of polaron formation is of interest for applications that employ polarons for charge separation and those that would benefit from carrier mobility offered by the suppression of polaron formation. Tuning spin properties and the exchange integral of these materials presents additional variables for controlling polaron formation in this class of highly polar materials. From a materials engineering perspective, polaronic tunability merits further study in intermediate and Mott−Hubbard insulating transition metal oxide materials.

ASSOCIATED CONTENT

Supporting Information

The Supporting Information is available free of charge at https://pubs.acs.org/doi/10.1021/jacs.4c16837.

$GdFeO_3$ characterization, detailed descriptions of the transient XUV spectrometer, and ab initio modeling; long time-scale XUV spectra and fitting of polaron shifts (PDF)

AUTHOR INFORMATION

Corresponding Author

Scott K. Cushing − *Division of Chemistry and Chemical Engineering, California Institute of Technology, Pasadena, California 91125, United States*; Email: scushing@caltech.edu

Authors

Jocelyn L. Mendes − *Division of Chemistry and Chemical Engineering, California Institute of Technology, Pasadena, California 91125, United States*

Hyun Jun Shin − *Department of Physics, Yonsei University, Seoul 03722, Republic of Korea*

Jae Yeon Seo − *Department of Physics, Yonsei University, Seoul 03722, Republic of Korea*

Nara Lee − *Department of Physics, Yonsei University, Seoul 03722, Republic of Korea*

Young Jai Choi − *Department of Physics, Yonsei University, Seoul 03722, Republic of Korea*

Joel B. Varley − *Lawrence Livermore National Laboratory, Livermore, California 94550, United States*; orcid.org/0000-0002-5384-5248

Complete contact information is available at: https://pubs.acs.org/10.1021/jacs.4c16837

Notes

The authors declare no competing financial interest.

ACKNOWLEDGMENTS

The authors thank Professor Hanzhe Liu, Dr. Jonathan Michelsen, and Levi Palmer for guidance and MATLAB scripts for performing the OCEAN calculations. This material is based on work performed by the Liquid Sunlight Alliance, which is supported by the U.S. Department of Energy, Office of Science, Office of Basic Energy Sciences, Fuels from Sunlight Hub, under award number DE-SC0021266. This research used resources of the National Energy Research Scientific Computing Center, a DOE Office of Science User Facility supported by the Office of Science of the U.S. Department of Energy under contract no. DE-AC02-05CH11231 using NERSC award BES-ERCAP0024109. The computations presented here were, in part, conducted in the Resnick High Performance Computing Center, a facility supported by the Resnick Sustainability Institute at the California Institute of Technology. The ground-state optical absorption of $GdFeO_3$ was collected at the Molecular Materials Research Center in the Beckman Institute of the California Institute of Technology. Fluorescence lifetime measurements were performed in the Caltech Biological Imaging Center, with the support of the Caltech Beckman Institute and the Arnold and Mabel Beckman Foundation. J.L.M. acknowledges support by the National Science Foundation Graduate Research Fellowship Program under grant no. 1745301. $GdFeO_3$ synthesis and characterization carried out at Yonsei University was supported by the National Research Foundation of Korea (NRF) through grants NRF-2021R1A2C1006375 and NRF-2022R1A2C1006740. The work of J.B.V. was performed under the auspices of the US DOE by Lawrence Livermore National Laboratory under contract DE-AC52-07NA27344 and supported by the HydroGEN Advanced Water Splitting Materials Consortium, established as part of the Energy Materials Network under the U.S. Department of Energy (DOE), the Office of Energy Efficiency and Renewable Energy (EERE), and the Hydrogen and Fuel Cell Technologies Office (HFTO).

REFERENCES

(1) Franchini, C.; Reticcioli, M.; Setvin, M.; Diebold, U. Polarons in Materials. *Nat. Rev. Mater.* **2021**, *6* (7), 560−586.

(2) Cheng, C.; Zhou, Z.; Long, R. Time-Domain View of Polaron Dynamics in Metal Oxide Photocatalysts. *J. Phys. Chem. Lett.* **2023**, *14* (49), 10988−10998.

(3) Suntivich, J.; Hautier, G.; Dabo, I.; Crumlin, E. J.; Kumar, D.; Cuk, T. Probing Intermediate Configurations of Oxygen Evolution Catalysis across the Light Spectrum. *Nat. Energy* **2024**, *9*, 1191−1198.

(4) Rettie, A. J. E.; Chemelewski, W. D.; Emin, D.; Mullins, C. B. Unravelling Small-Polaron Transport in Metal Oxide Photoelectrodes. *J. Phys. Chem. Lett.* **2016**, *7* (3), 471−479.

(5) Pastor, E.; Sachs, M.; Selim, S.; Durrant, J. R.; Bakulin, A. A.; Walsh, A. Electronic Defects in Metal Oxide Photocatalysts. *Nat. Rev. Mater.* **2022**, *7* (7), 503−521.

(6) Emin, D.; *Polarons*; Cambridge University Press: 2012.

(7) Yazdani, N.; Bodnarchuk, M. I.; Bertolotti, F.; Masciocchi, N.; Fureraj, I.; Guzelturk, B.; Cotts, B. L.; Zajac, M.; Rainò, G.; Jansen, M.; Boehme, S. C.; Yarema, M.; Lin, M.-F.; Kozina, M.; Reid, A.; Shen, X.; Weathersby, S.; Wang, X.; Vauthey, E.; Guagliardi, A.; Kovalenko, M. V.; Wood, V.; Lindenberg, A. M. Coupling to Octahedral Tilts in Halide Perovskite Nanocrystals Induces Phonon-Mediated Attractive Interactions between Excitons. *Nat. Phys.* **2024**, *20* (1), 47−53.

(8) Ghosh, R.; Spano, F. C. Excitons and Polarons in Organic Materials. *Acc. Chem. Res.* **2020**, *53* (10), 2201−2211.

(9) Biswas, S.; Wallentine, S.; Bandaranayake, S.; Baker, L. R. Controlling Polaron Formation at Hematite Surfaces by Molecular Functionalization Probed by XUV Reflection-Absorption Spectroscopy. *J. Chem. Phys.* **2019**, *151* (10), 104701.

(10) Carneiro, L. M.; Cushing, S. K.; Liu, C.; Su, Y.; Yang, P.; Alivisatos, A. P.; Leone, S. R. Excitation-Wavelength-Dependent Small Polaron Trapping of Photoexcited Carriers in α-Fe_2O_3. *Nat. Mater.* **2017**, *16* (8), 819−825.

(11) Vura-Weis, J.; Jiang, C.-M.; Liu, C.; Gao, H.; Lucas, J. M.; de Groot, F. M. F.; Yang, P.; Alivisatos, A. P.; Leone, S. R. Femtosecond $M_{2,3}$-Edge Spectroscopy of Transition-Metal Oxides: Photoinduced Oxidation State Change in α-Fe_2O_3. *J. Phys. Chem. Lett.* **2013**, *4* (21), 3667−3671.

(12) Kim, Y.-J.; Mendes, J. L.; Michelsen, J. M.; Shin, H. J.; Lee, N.; Choi, Y. J.; Cushing, S. K. Coherent Charge Hopping Suppresses Photoexcited Small Polarons in $ErFeO_3$ by Antiadiabatic Formation Mechanism. *Sci. Adv.* **2024**, *10*, No. eadk4282.

(13) Bandaranayake, S.; Hruska, E.; Londo, S.; Biswas, S.; Baker, L. R. Small Polarons and Surface Defects in Metal Oxide Photocatalysts Studied Using XUV Reflection-Absorption Spectroscopy. *J. Phys. Chem. C* **2020**, *124* (42), 22853−22870.

(14) Husek, J.; Cirri, A.; Biswas, S.; Baker, L. R. Surface Electron Dynamics in Hematite (α-Fe_2O_3): Correlation Between Ultrafast Surface Electron Trapping and Small Polaron Formation. *Chem. Sci.* **2017**, *8* (12), 8170−8178.

(15) Gajapathy, H.; Bandaranayake, S.; Hruska, E.; Vadakkayil, A.; Bloom, B. P.; Londo, S.; McClellan, J.; Guo, J.; Russell, D.; de Groot, F. M. F.; Yang, F.; Waldeck, D. H.; Schultze, M.; Baker, L. R. Spin Polarized Electron Dynamics Enhance Water Splitting Efficiency by Yttrium Iron Garnet Photoanodes: A New Platform for Spin Selective Photocatalysis. *Chem. Sci.* **2024**, *15* (9), 3300−3310.

(16) Bu, X.; Li, Y. Optical Signature for Distinguishing between Mott-Hubbard, Intermediate, and Charge-Transfer Insulators. *Phys. Rev. B* **2022**, *106* (24), L241101.

(17) Zhu, X.-H.; Xiao, X.-B.; Chen, X.-R.; Liu, B.-G. Electronic Structure, Magnetism and Optical Properties of Orthorhombic $GdFeO_3$ from First Principles. *RSC Adv.* **2017**, *7* (7), 4054−4061.

(18) Khan, H.; Ahmad, T. Perspectives and Scope of ABO_3 Type Multiferroic Rare-Earth Perovskites. *Chin. J. Phys.* **2024**, *91*, 199−219.

(19) Podlesnyak, A.; Nikitin, S. E.; Ehlers, G. Low-Energy Spin Dynamics in Rare-Earth Perovskite Oxides. *J. Phys. Condens. Matter* **2021**, *33* (40), 403001.

(20) Liu, H.; Michelsen, J. M.; Mendes, J. L.; Klein, I. M.; Bauers, S. R.; Evans, J. M.; Zakutayev, A.; Cushing, S. K. Measuring Photoexcited Electron and Hole Dynamics in ZnTe and Modeling Excited State Core-Valence Effects in Transient Extreme Ultraviolet Reflection Spectroscopy. *J. Phys. Chem. Lett.* **2023**, *14*, 2106−2111.

(21) Klein, I. M.; Liu, H.; Nimlos, D.; Krotz, A.; Cushing, S. K. Ab Initio Prediction of Excited-State and Polaron Effects in Transient XUV Measurements of α-Fe_2O_3. *J. Am. Chem. Soc.* **2022**, *144* (28), 12834−12841.

(22) Giannozzi, P.; Baroni, S.; Bonini, N.; Calandra, M.; Car, R.; Cavazzoni, C.; Ceresoli, D.; Chiarotti, G. L.; Cococcioni, M.; Dabo, I.; et al. QUANTUM ESPRESSO: A Modular and Open-Source Software Project for Quantum Simulations of Materials. *J. Phys. Condens. Matter* **2009**, *21* (39), 395502.

(23) Giannozzi, P.; Andreussi, O.; Brumme, T.; Bunau, O.; Buongiorno Nardelli, M.; Calandra, M.; Car, R.; Cavazzoni, C.; Ceresoli, D.; Cococcioni, M.; Colonna, N.; Carnimeo, I.; Dal Corso, A.; de Gironcoli, S.; Delugas, P.; DiStasio, R. A.; Ferretti, A.; Floris, A.; Fratesi, G.; Fugallo, G.; Gebauer, R.; Gerstmann, U.; Giustino, F.; Gorni, T.; Jia, J.; Kawamura, M.; Ko, H.-Y.; Kokalj, A.; Küçükbenli, E.; Lazzeri, M.; Marsili, M.; Marzari, N.; Mauri, F.; Nguyen, N. L.; Nguyen, H.-V.; Otero-de-la-Roza, A.; Paulatto, L.; Poncé, S.; Rocca, D.; Sabatini, R.; Santra, B.; Schlipf, M.; Seitsonen, A. P.; Smogunov, A.; Timrov, I.; Thonhauser, T.; Umari, P.; Vast, N.; Wu, X.; Baroni, S. Advanced Capabilities for Materials Modelling with Quantum ESPRESSO. *J. Phys. Condens. Matter* **2017**, *29* (46), 465901.

(24) Vinson, J. Advances in the OCEAN-3 Spectroscopy Package. *Phys. Chem. Chem. Phys.* **2022**, *24* (21), 12787−12803.

(25) Vinson, J.; Rehr, J. J.; Kas, J. J.; Shirley, E. L. Bethe-Salpeter Equation Calculations of Core Excitation Spectra. *Phys. Rev. B* **2011**, *83* (11), 115106.

(26) Gilmore, K.; Vinson, J.; Shirley, E. L.; Prendergast, D.; Pemmaraju, C. D.; Kas, J. J.; Vila, F. D.; Rehr, J. J. Efficient Implementation of Core-Excitation Bethe−Salpeter Equation Calculations. *Comput. Phys. Commun.* **2015**, *197*, 109−117.

(27) Klein, I. M.; Krotz, A.; Lee, W.; Michelsen, J. M.; Cushing, S. K. Ab Initio Calculations of XUV Ground and Excited States for First-Row Transition Metal Oxides. *J. Phys. Chem. C* **2023**, *127* (2), 1077−1086.

(28) Sadigh, B.; Erhart, P.; Åberg, D. Variational Polaron Self-Interaction-Corrected Total-Energy Functional for Charge Excitations in Insulators. *Phys. Rev. B* **2015**, *92* (7), 075202.

(29) Heyd, J.; Scuseria, G. E.; Ernzerhof, M. Hybrid Functionals Based on a Screened Coulomb Potential. *J. Chem. Phys.* **2003**, *118* (18), 8207−8215.

(30) Zhou, F.; Sadigh, B.; Erhart, P.; Åberg, D. Ab Initio Prediction of Fast Non-Equilibrium Transport of Nascent Polarons in SrI_2: A Key to High-Performance Scintillation. *npj Comput. Mater.* **2016**, *2* (1), 1−7.

(31) Paier, J.; Marsman, M.; Hummer, K.; Kresse, G.; Gerber, I. C.; Angyan, J. G. Screened Hybrid Density Functionals Applied to Solids. *J. Chem. Phys.* **2006**, *124*, 154709.

(32) Varley, J. B.; Janotti, A.; Franchini, C.; Van de Walle, C. G. Role of Self-Trapping in Luminescence and *p*-Type Conductivity of Wide-Band-Gap Oxides. *Phys. Rev. B* **2012**, *85* (8), 081109.

(33) Li, H.; Chen, Y.; Xi, S.; Wang, J.; Sun, S.; Sun, Y.; Du, Y.; Xu, Z. J. Degree of Geometric Tilting Determines the Activity of FeO_6 Octahedra for Water Oxidation. *Chem. Mater.* **2018**, *30* (13), 4313−4320.

(34) Cashion, J. D.; Cooke, A. H.; Martin, D. M.; Wells, M. R. Magnetic Interactions in Gadolinium Orthoferrite. *J. Phys. C: Solid State Phys.* **1970**, *3* (7), 1612.

(35) Das, M.; Roy, S.; Mandal, P. Giant Reversible Magnetocaloric Effect in a Multiferroic $GdFeO_3$ Single Crystal. *Phys. Rev. B* **2017**, *96* (17), 174405.

(36) Paul, P.; Ghosh, P. S.; Rajarajan, A. K.; Babu, P. D.; Rao, T. V. C. Ground State Spin Structure of $GdFeO_3$: A Computational and Experimental Study. *J. Magn. Magn. Mater.* **2021**, *518*, 167407.

(37) Yuan, X.; Sun, Y.; Xu, M. Effect of Gd Substitution on the Structure and Magnetic Properties of $YFeO_3$ Ceramics. *J. Solid State Chem.* **2012**, *196*, 362−366.
(38) Shah, J.; Kotnala, R. K. Room Temperature Magnetoelectric Coupling Enhancement in Mg-Substituted Polycrystalline $GdFeO_3$. *Scr. Mater.* **2012**, *67* (4), 316−319.
(39) Mikhaylovskiy, R. V.; Huisman, T. J.; Gavrichkov, V. A.; Polukeev, S. I.; Ovchinnikov, S. G.; Afanasiev, D.; Pisarev, R. V.; Rasing, T.; Kimel, A. V. Resonant Pumping of $d - d$ Crystal Field Electronic Transitions as a Mechanism of Ultrafast Optical Control of the Exchange Interactions in Iron Oxides. *Phys. Rev. Lett.* **2020**, *125* (15), 157201.
(40) Chatterjee, J.; Das, A. N. Role of the Superexchange Interaction in Magnetic Transition and Polaron Crossover. *Physica. B: Condens. Matter* **2004**, *384* (1), 89−94.
(41) Li, S.; Johnston, S. Suppressed Superexchange Interactions in the Cuprates by Bond-Stretching Oxygen Phonons. *Phys. Rev. B* **2023**, *108* (20), L201113.
(42) Mentink, J. H.; Balzer, K.; Eckstein, M. Ultrafast and Reversible Control of the Exchange Interaction in Mott Insulators. *Nat. Commun.* **2015**, *6* (1), 6708.
(43) Berger, E.; Valášek, P.; Von Der Linden, W. Two-Dimensional Hubbard−Holstein Model. *Phys. Rev. B* **1995**, *52* (7), 4806−4814.
(44) Hubbard, J. Electron Correlations in Narrow Energy Bands. *Proc. R. Soc. London, Ser. A* **1963**, *276*, 238−257.
(45) Holstein, T. Studies of Polaron Motion: Part I. The Molecular-Crystal Model. *Ann. Phys.* **1959**, *8* (3), 325−342.
(46) Anderson, P. W. New Approach to the Theory of Superexchange Interactions. *Phys. Rev.* **1959**, *115* (1), 2−13.
(47) Cappelluti, E.; Ciuchi, S.; Fratini, S. Polaronic Features in the Optical Properties of the Holstein *t-J* Model. *Phys. Rev. B* **2007**, *76* (12), 125111.
(48) Fehske, H.; Roder, H.; Mistriotis, A.; Buttner, H. The Phase Diagram of the 2D Holstein-t-J Model Near Half Filling. *J. Phys.: Condens. Matter* **1993**, *5* (22), 3565.
(49) Pavarini, E.; Koch, E. Origin of Jahn−Teller Distortion and Orbital Order in $LaMnO_3$. *Phys. Rev. Lett.* **2010**, *104* (8), 086402.
(50) Endres, H.; Noack, R. M.; Hanke, W.; Poilblanc, D.; Scalapino, D. J. Dynamical Properties of Two Coupled Hubbard Chains at Half-Filling. *Phys. Rev. B* **1996**, *53* (9), 5530−5540.
(51) Panuganti, S.; Cuthriell, S. A.; Leonard, A. A.; Quintero, M. A.; Laing, C. C.; Guzelturk, B.; Zhang, X.; Chen, L. X.; Kanatzidis, M. G.; Schaller, R. D. Transient X-Ray Diffraction Reveals Nonequilibrium Phase Transition in Thin Films of $CH_3NH_3PbI_3$ Perovskite. *ACS Energy Lett.* **2023**, *8* (1), 691−698.
(52) Zhang, J.; Shi, J.; Chen, Y.; Zhang, K. H. L.; Yang, Y. Bimolecular Self-Trapped Exciton Formation in Bismuth Vanadate. *J. Phys. Chem. Lett.* **2022**, *13* (42), 9815−9821.
(53) Jiang, C.-M.; Baker, L. R.; Lucas, J. M.; Vura-Weis, J.; Alivisatos, A. P.; Leone, S. R. Characterization of Photo-Induced Charge Transfer and Hot Carrier Relaxation Pathways in Spinel Cobalt Oxide (Co_3O_4). *J. Phys. Chem. C* **2014**, *118* (39), 22774−22784.
(54) Molesky, I. J. P.; Lee, A.; Cushing, S. K.; Chang, H.-T.; Ondry, J. C.; Alivisatos, A. P.; Leone, S. R. Characterization of Carrier Cooling Bottleneck in Silicon Nanoparticles by Extreme Ultraviolet (XUV) Transient Absorption Spectroscopy. *J. Phys. Chem. C* **2021**, *125* (17), 9319−9329.
(55) Verkamp, M.; Leveillee, J.; Sharma, A.; Lin, M.-F.; Schleife, A.; Vura-Weis, J. Carrier-Specific Hot Phonon Bottleneck in $CH_3NH_3PbI_3$ Revealed by Femtosecond XUV Absorption. *J. Am. Chem. Soc.* **2021**, *143* (48), 20176−20182.
(56) Stavitski, E.; de Groot, F. M. F. The CTM4XAS Program for EELS and XAS Spectral Shape Analysis of Transition Metal L Edges. *Micron* **2010**, *41* (7), 687−694.
(57) Panneerselvam, I. R.; Baldo, C., III; Sahasranaman, M.; Murugesan, S.; Rangaswamy, N.; Pai, S. D. K. R.; Selvarathinam, Y. Large Power Factors in Wide Band Gap Semiconducting $RFeO_3$ Materials for High-Temperature Thermoelectric Applications. *ACS Appl. Energy Mater.* **2020**, *3* (11), 11193−11205.
(58) Gu, X.; Fan, Z.; Bao, H.; Zhao, C. Y. Revisiting Phonon-Phonon Scattering in Single-Layer Graphene. *Phys. Rev. B* **2019**, *100* (6), 064306.
(59) Endo, M.; Kimura, S.; Tani, S.; Kobayashi, Y. Coherent Control of Acoustic Phonons in a Silica Fiber Using a Multi-GHz Optical Frequency Comb. *Commun. Phys.* **2021**, *4* (1), 1−8.
(60) Khalil, M.; Marcus, M. A.; Smeigh, A. L.; McCusker, J. K.; Chong, H. H. W.; Schoenlein, R. W. Picosecond X-Ray Absorption Spectroscopy of a Photoinduced Iron(II) Spin Crossover Reaction in Solution. *J. Phys. Chem. A* **2006**, *110* (1), 38−44.
(61) Zhang, K.; Ash, R.; Girolami, G. S.; Vura-Weis, J. Tracking the Metal-Centered Triplet in Photoinduced Spin Crossover of Fe-$(Phen)_3^{2+}$ with Tabletop Femtosecond M-Edge X-Ray Absorption Near-Edge Structure Spectroscopy. *J. Am. Chem. Soc.* **2019**, *141* (43), 17180−17188.
(62) Occhialini, C. A.; Tseng, Y.; Elnaggar, H.; Song, Q.; Blei, M.; Tongay, S. A.; Bisogni, V.; de Groot, F. M. F.; Pelliciari, J.; Comin, R. Nature of Excitons and Their Ligand-Mediated Delocalization in Nickel Dihalide Charge-Transfer Insulators. *Phys. Rev. X* **2024**, *14* (3), 031007.
(63) Takubo, K.; Mizokawa, T.; Son, J.-Y.; Nambu, Y.; Nakatsuji, S.; Maeno, Y. Unusual Superexchange Pathways in an NiS_2 Triangular Lattice with Negative Charge-Transfer Energy. *Phys. Rev. Lett.* **2007**, *99* (3), 037203.
(64) Takada, Y.; Masaki, M. Polarons in Jahn−Teller Crystals: Intrinsic Difference between e_g and t_{2g} Electrons. *J. Supercond. Nov. Magn.* **2007**, *20* (7), 629−633.
(65) Titus Samuel Sudandararaj, A.; Sathish Kumar, G.; Dhivya, M.; Eithiraj, R. D.; Banu, I. B. S. Band Structure Calculation and Rietveld Refinement of Nanoscale $GdFeO_3$ with Affirmation of Jahn Teller's Distortion on Electric and Magnetic Properties. *J. Alloys Compd.* **2019**, *783*, 393−398.
(66) Panchwanee, A.; Reddy, V. R.; Gupta, A.; Bharathi, A.; Phase, D. M. Study of Local Distortion and Spin Reorientation in Polycrystalline Mn Doped $GdFeO_3$. *J. Alloys Compd.* **2018**, *745*, 810−816.
(67) Kim, B. H.; Min, B. I. Nearest and Next-Nearest Superexchange Interactions in Orthorhombic Perovskite Manganites $RMnO_3$ (R = Rare Earth). *Phys. Rev. B* **2009**, *80* (6), 064416.
(68) Mikhaylovskiy, R. V.; Hendry, E.; Secchi, A.; Mentink, J. H.; Eckstein, M.; Wu, A.; Pisarev, R. V.; Kruglyak, V. V.; Katsnelson, M. I.; Rasing, T.; Kimel, A. V. Ultrafast Optical Modification of Exchange Interactions in Iron Oxides. *Nat. Commun.* **2015**, *6* (1), 8190.
(69) Feinberg, D.; Germain, P.; Grilli, M.; Seibold, G. Joint Superexchange−Jahn−Teller Mechanism for Layered Antiferromagnetism in $LaMnO_3$. *Phys. Rev. B* **1998**, *57* (10), R5583−R5586.
(70) Anderson, P. W. Antiferromagnetism. Theory of Superexchange Interaction. *Phys. Rev.* **1950**, *79* (2), 350−356.
(71) Zhou, J.-S.; Alonso, J. A.; Pomjakushin, V.; Goodenough, J. B.; Ren, Y.; Yan, J.-Q.; Cheng, J.-G. Intrinsic Structural Distortion and Superexchange Interaction in the Orthorhombic Rare-Earth Perovskites $RCrO_3$. *Phys. Rev. B* **2010**, *81* (21), 214115.
(72) Zhou, J.-S.; Goodenough, J. B. Intrinsic Structural Distortion in Orthorhombic Perovskite Oxides. *Phys. Rev. B* **2008**, *77* (13), 132104.
(73) Eibschütz, M.; Shtrikman, S.; Treves, D. Mössbauer Studies of Fe^{57} in Orthoferrites. *Phys. Rev.* **1967**, *156* (2), 562−577.